# Perylene radical cation salts with a five-eighths-filled conduction band: An ESR analysis

A. Wolter, U. Fasol, R. Jäppelt, and E. Dormann
*Physikalisches Institut, Universität Karlsruhe(TH), D-76128 Karlsruhe, Germany*
(Received 16 February 1996; revised manuscript received 10 June 1996)

The quasi-one-dimensional conductors $(PE)_2PF_6 \cdot \frac{2}{3}THF$ and $(PE)_2AsF_6 \cdot \frac{2}{3}THF$ (PE = perylene, THF = tetrahydrofuran) undergo a Peierls transition at $T_P = 118$ K and 102 K, respectively. We present specific-heat data and a detailed electron-spin-resonance (ESR) study of the metallic high-temperature and the semiconducting low-temperature phase (linewidth, intensity, $g$ tensor, 9.5 GHz, and 415 MHz). Above $T_P$ motional and exchange narrowings in conjunction with the high one dimensionality account for the extremely small width ($\Delta B \simeq 10$ mG) of the Lorentzian conduction electron line. Due to the small linewidth, the $g$ tensor can be determined with high precision. This allows us to follow the reorientation of the perylene stacks in the course of a structural phase transition in the metallic range. Far below $T_P$ spectra consist of the lines of several defect types. In the intermediate temperature range near below $T_P$, where defects and conduction electrons contribute to the ESR intensity, the linewidth was analyzed as a function of temperature and orientation. Two of the defect types are found to interact (magnetic dipole-dipole, exchange) with the conduction electrons. Strong exchange coupling leads to a bottleneck situation, which together with a Korringa-type relaxation of the defects accounts for the pronounced increase in linewidth below $T_P$. We propose the different nature, i.e., localized at a chain end or solitonlike and mobile, of the defect spins to be responsible for the different temperature dependences of the width of the associated lines. [S0163-1829(96)05141-7]

## I. INTRODUCTION

The rich variety of low-temperature ground states has caused the unceasing interest that molecule-based quasi-one-dimensional conductors have obtained in recent years.[1] Spin-density-wave (SDW) and charge-density-wave (CDW) condensation and their competition with superconducting ground states continue to fascinate a small, but active community of solid-state physicists and chemists.[2,3] In the ever-growing family of molecule-based quasi-one-dimensional conductors, the salts built up by radical cations of simple arenes (flat, pure hydrocarbons like naphthalene, fluoranthene, or perylene) and inorganic complex anions like hexafluorophosphate ($PF_6$) or hexafluoroarsenate ($AsF_6$) exhibit a number of peculiarities: They seem to have a very weak electron-electron interaction and show pure CDW ground states.[4–7] They display an especially high degree of anisotropy of the spin- and charge-carrier motion.[8,9] But most of all, the interplay of weak spin-orbit coupling (due to the conduction electrons residing only on light atoms) and one dimensionality of the carrier motion on separated stacks results in an extremely narrow electron-spin-resonance (ESR) linewidth of the conduction electrons.[10] Thus magnetic resonance techniques have unparalleled potentiality for the characterization of electronic structure and spin dynamics of these radical cation salts,[8,11,12]

Like the well-known Bechgard salts[3], most of the quasi-one-dimensional organic metals studied until now have a 2:1 stoichiometry of aromatic molecules and singly charged diamagnetic anions. Consequently, and neglecting details, the conduction-electron band is three-quarters filled. Thus, the Peierls transition opening an energy gap at the Fermi energy is accompanied by the rearrangement of uniform or dimerized stacks into units of four molecules in the stacking direction.

In an attempt to realize smaller $2k_F$ values and thus larger rearranged units in the low-temperature phase, we electrocrystallized the radical cation salts $(perylene)_2X \cdot \frac{2}{3}$ tetrahydrofuran [abbreviated in the following as $(PE)_2X \cdot \frac{2}{3}$ THF], with $X = PF_6$, $AsF_6$, or mixtures of both counterions. According to an analysis of various PE radical cation salts by Endres *et al.*,[13] these salts contain two different groups of PE molecules. The molecular packing is shown in Fig. 1.[14] Per unit cell, there are four PE molecules (''tetramer'') in the conductive stack ($c$ direction) and two in the ''walls'' of this stack. Three counterions and two partially disordered solvent molecules belong also to the unit cell. We will give further evidence in Sec. III A 1 below that only the PE molecules in

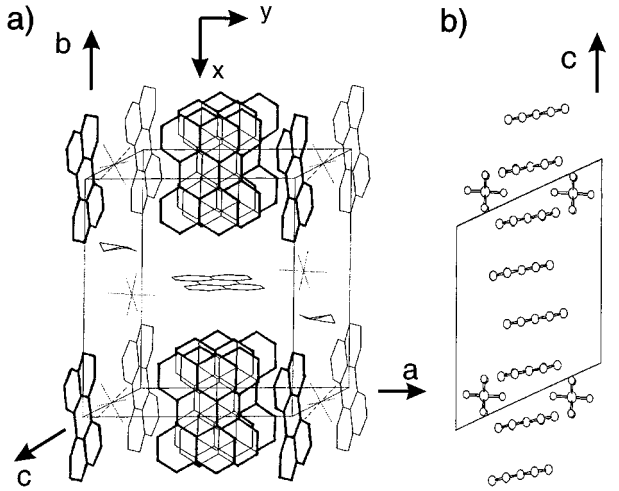


FIG. 1. Molecular packing in $(PE)_2X \cdot \frac{2}{3}THF$, seen along stacking direction $c$ [part (a)] or along $b$ [part (b)], i.e., perpendicular to the stacking direction (Ref. 14). Crystallographic directions $a$, $b$, and $c$ and main axes of the $g$ tensor are indicated in (a).

 

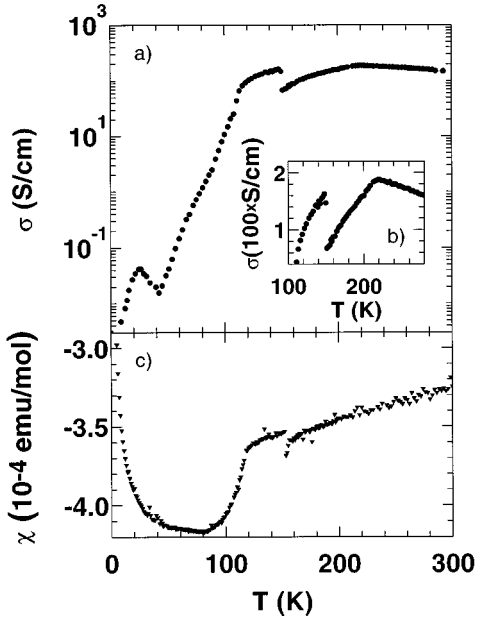


FIG. 2. (a) Microwave conductivity parallel to stacking direction $c$ as function of temperature for $(PE)_2PF_6 \cdot \frac{2}{3}THF$, (b) data of (a) on an expanded linear scale for $T$ between 100 K and 280 K, and (c) static magnetic susceptibility for $(PE)_2PF_6 \cdot \frac{2}{3}THF$ (unoriented bundle) measured with a superconducting quantum interference device (SQUID) magnetometer.

the stack carry charge and spin. Thus, these quasi-one-dimensional conductors have a *five-eighths*-filled conduction band in the extended band scheme, neglecting dimerization or tetramerization.[14] In the reduced zone scheme, the third band is half-filled with small $k_F = \pi/2c$ ($c \simeq 13.8$ Å).

As is typical for quasi-one-dimensional conductors built from pure hydrocarbon radical cations, these salts show a conduction electron (CE) ESR line of only about 10 mG width in the metallic phase, which can be exploited by cw and pulse techniques.[18,15,16] Low-frequency pulsed ESR in a static magnetic field gradient allowed the determination of the anisotropy of the spin (and charge) carrier diffusion constant of $D_{||}/D_{\perp} \geqslant 1500$.[17]

As shown in Fig. 2,[14] these quasi-one-dimensional organic conductors show a Peierls transition at $T_P = 118 \pm 2$ K for $X = PF_6$ ($102 \pm 2$ K for $X = AsF_6$), which is accompanied by the decrease of electrical conductivity and Pauli-paramagnetic susceptibility. Characteristics of CDW transport were observed in the low-temperature phase.[7] The paramagnetic defects, responsible for the low-temperature Curie tail, will be analyzed below. Also, additional anomalies observed in the high-temperature metallic phase (Fig. 2) will be elucidated in the present ESR analysis.

Our report is organized as follows. Crystal growth, ESR, and specific-heat measuring techniques are characterized in Sec. II. Experimental results on the conduction-band filling, ESR-line shape, and structural phase transition at $T_r$ for the metallic range are presented in Sec. III A. The phenomena observed accompanying the Peierls transition are reported in Sec. III B. Defects in the molecular stacks are of particular importance in quasi-one-dimensional conductors. Therefore, information on the paramagnetic defects accessible via ESR is analyzed in Sec. III C. The conduction electrons can be ''switched on'' by increasing the measurement temperature in the low-temperature nonmetallic phase of these PE salts. Thus the interaction of defect and CE spins can be in detail analyzed (Sec. III D). The statements relying on the application of appropriate theoretical models will be reported in Sec. IV. Thus the current results allow a classification of the structural phase transition in the metallic range (Sec. IV A). Furthermore, a quantitative picture of the spin dynamics of coexisting defect and CE spins is presented in Sec. IV B, followed by the conclusions in Sec. V.

## II. EXPERIMENTAL DETAILS

### A. Crystal growth

Electrocrystallization of $(PE)_2X \cdot \frac{2}{3}THF$ (with $X = PF_6$ or $AsF_6$) was performed by anodic oxidation in a three-compartment electrochemical cell at 15 or 16 °C. Therefore 350 mg zone refined perylene (PE) and 1 g $Bu_4NPF_6$ (for $X = PF_6$), respectively, 1.112 g $Bu_4NAsF_6$ (for $X = AsF_6$), were dissolved in 100 ml tetrahydrofuran (THF), resulting in a saturated solution. Using platinum-foil electrodes and a constant voltage of 3 or 4 V for 24 or 48 h typically 20 mg of crystals with glossy-black natural surfaces were obtained.[13,14]

The needlelike crystals were stable at reduced temperatures for extended periods of time, but showed signs of decomposition after extended time in air at room temperature. The glossy surfaces became dull, the signal intensity of the narrow ESR line at room temperature decreased by about 20% in 48 h, and the number of Curie-paramagnetic defects increased.

General composition of the crystals was controlled by chemical elemental analysis. Deviations from the nominal compositional ratio of 2:1 reside clearly below 3%.

Results of two different crystals with $X = AsF_6$ are shown. They were grown under slightly different conditions: (a) $U = 4$ V, $t = 24$ h, $T = 16$ °C and (b) $U = 3$ V, $t = 48$ h, $T = 15$ °C. If there are no appropriate remarks in a figure, the measurements were performed with the crystal grown under (a).

### B. Electron spin resonance

#### *1. Microwave range*

Most ESR measurements were performed at the $X$ band on a BRUKER ESP 300E spectrometer, equipped with a field-frequency lock, using a $TE_{102}$ mode cavity ($Q = 3500$) and an Oxford Instruments variable temperature setup. Temperature stability during measurement was better than $\pm 0.1$ K, but the absolute error may amount up to 6 K, depending on temperature range and gas flow. The angular dependence of the $g$ value, linewidth, and intensity could be analyzed for rotation of the crystals by 360° around an axis perpendicular to the field direction. $(Fluoranthene)_2PF_6$ crystals, whose $g$ factor had been measured[21] with an accuracy of $\pm 1.5 \times 10^{-5}$, were used to determine the absolute values of the $g$ factor. The relative accuracy due to the inhomogeneity of the static magnetic field was better than $5 \times 10^{-6}$. The variation of the $g$ factor with the orientation in the static magnetic field could be described by

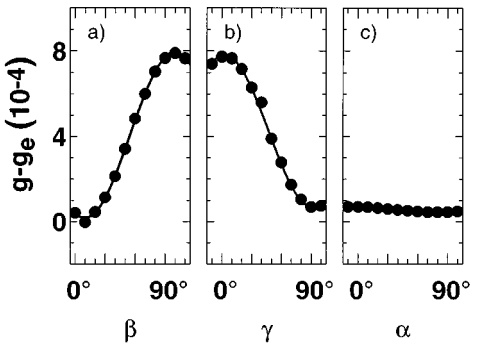


FIG. 3. Anisotropy of the $g$ factor for $X = PF_6$: (a) The crystal was turned from $\mathbf{B}_0 \| c$ to $\mathbf{B}_0 \perp b$ and $c$, (b) rotation with $c$ as axis of rotation, (c) the crystal was turned from $\mathbf{B}_0 \| b$ back to $\mathbf{B}_0 \| c$. The solid lines are fits of Eq. (1); for parameters see Table I ($g_e = 2.002\,32$).

$$g = \sqrt{g_{xx}^2 \cos^2(\vartheta_x) + g_{yy}^2 \cos^2(\vartheta_y) + g_{zz}^2 \cos^2(\vartheta_z)}. \qquad (1)$$

$g_{ii}$ is the principal value of the $g$ tensor, and $\vartheta_i$ is the angle between the principal axis **i** (Fig. 1) and the static magnetic field.

#### *2. Radio frequency range*

Radio frequency ESR results were obtained on a home-built homodyne-bridge type spectrometer operating at 415 MHz (Ref. 18) using an helical coil resonator ($Q = 150$), Oxford Instruments variable temperature cryostat (type CF1200), and water-cooled Helmholtz coils for generation of the static magnetic field. Again a relative temperature accuracy of $\pm 0.1$ K was realized. The sample temperature was verified by a second thermocouple. So the absolute temperature error was generally below $\pm 1$ K at this setup. For the analysis of the angular dependence, the crystals could be rotated by 360° around an axis perpendicular to the static field direction.

### C. Specific-heat measurement

The molar heat capacity of perylene salts was measured by the continuous heating method[19,20] with typical heating rates of about 17 mK/s. Every 0.5 s temperatures of the sample and surrounding heat shields were measured to guarantee the aspired equalness of the temperature. The mass of the sample consisting of about 10–15 tiny needlelike crystals was 9.6 mg for $X = PF_6$ and 7.9 mg for $X = AsF_6$. The needles were fixed with a precisely known amount of Apiezon N at the sample holder. Reproducibility and independence on heating rate were verified.[20]

## III. DISCUSSION OF THE EXPERIMENTAL RESULTS

### A. Metallic range

Orientation and anisotropy of the CE ESR $g$ tensor proves the 5/8 conduction band filling and reveals the molecular reorientation at the structural phase transition, $T_r$.

#### *1. Conduction band filling*

Figure 3 shows the variation of the CE $g$ factor with the orientation in the static magnetic field ($\mathbf{B}_0$). In Table I the results for $X = PF_6$ and $X = AsF_6$ are compared with those for $(PE)_6PF_6$. The latter salt is not metallic and only one PE dimer carries the electron spin.[22,23] In spite of the different structures and stoichiometries all three salts show nearly the same principal values and anisotropy of the $g$ tensor. This proves that the observed $g$ tensor of the $(PE)_2X \cdot \frac{2}{3}THF$ crystals is that of the PE molecules in the stack. It is interesting to note that the angle between the normal to the molecular plane and the $c$ axis of about 9.5°, known from x-ray analysis, can precisely be determined from the $\beta$ dependence of the $g$ value [see Fig. 3(a)]. Hence the two PE molecules of the ''wall'' (Fig. 1) must be electrically neutral. Therefore the three electrons required for the three counterions ($PF_6^-$ or $AsF_6^-$) per unit cell must be contributed by the four PE molecules of the stacks. Under these circumstances and neglecting dimerization and quaternization of the in-stack molecules, we obtain a five-eighths-filled conduction band as mentioned in the Introduction.

TABLE I. Differences between the principal values of the $g$ tensor and the $g$ factor of free electrons $g_e = 2.002\,32$ and differences between the principal values themselves for $(PE)_2X \cdot \frac{2}{3}THF$ with $X = PF_6$, $X = AsF_6$ and for $(PE)_6PF_6$ (Ref. 23) (absolute error $\pm 2 \times 10^{-5}$).

| | $X = PF_6$ | $X = AsF_6$ | $(PE)_6PF_6$ |
|---|---|---|---|
| $(g_{yy} - g_e)$ $(10^{-5})$ | 70 | 72 | 64 |
| $(g_{xx} - g_e)$ $(10^{-5})$ | −4 | −1 | −6 |
| $(g_{zz} - g_e)$ $(10^{-5})$ | −7 | −6 | −9 |
| $(g_{yy} - g_{zz})$ $(10^{-5})$ | 77 | 78 | 73 |
| $(g_{zz} - g_{xx})$ $(10^{-5})$ | −3 | −5 | −3 |
| $(g_{xx} - g_{yy})$ $(10^{-5})$ | −74 | −73 | −70 |

#### *2. Electron spin resonance linewidth and line shape*

In spite of the one dimensionality of the electrical conductivity in the metallic range the ESR lines of the $(PE)_2X \cdot \frac{2}{3}THF$ salts are of Lorentzian shape. The familiar possibility[24] to test graphically whether the shape of the line

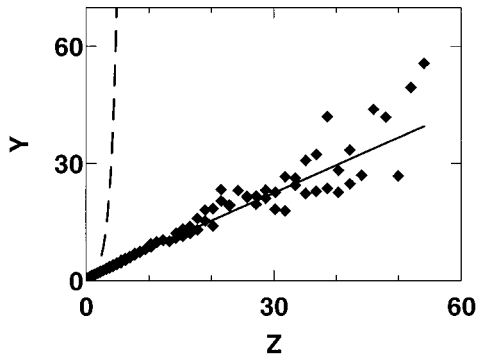


FIG. 4. Analysis of the ESR line shape for $X = PF_6$ at 120 K by plotting the weighted inverse signal strength ($Y$) vs normalized distance from the line center ($z$) [see Eqs. (2) and (3)]. For a perfect Lorentzian ESR line shape the straight solid line would be expected and is observed. The dotted line would be expected for a Gaussian line shape.

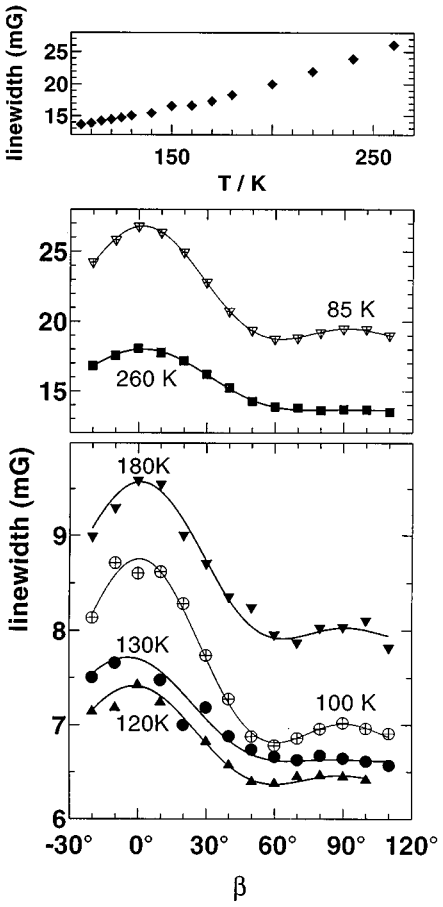


FIG. 5. Variation of the ESR linewidth with orientation and temperature for $(PE)_2AsF_6 \cdot \frac{2}{3}THF$. The linewidths given in the small figure at the top are results of measurements with $c \| \mathbf{B}_0$ at 9.45 GHz in the metallic range. The dependence of the orientation was obtained in measurements at 415 MHz. The maximum appears if the static magnetic field is parallel to the stacking direction *c*. The axis of rotation was *b*. Solid (open) symbols for temperatures above (below) $T_P$. The solid lines are fitted curves (see text).

is Lorentzian or not is shown in Fig. 4. If $F^i(B-B_0)$ is the first derivative of the theoretical shape function (Lorentzian, $i=L$; Gaussian, $i=G$) and

$$y^i := \sqrt{\frac{F^i_{\max}}{|F^i|}\frac{|B-B_0|}{\Delta B_{\text{p.p.}}}} \quad \text{and} \quad z := \left(\frac{B-B_0}{\Delta B_{\text{p.p.}}}\right)^2, \qquad (2)$$

with $B_0$ the field in the center of the line, then it is

$$y^L = \frac{1}{\sqrt{2}}\left(\frac{3}{4}+z\right) \quad \text{and} \quad y^G = (2\sqrt{e})^{-1/2}\exp(z). \qquad (3)$$

For ideally Lorentzian-shaped lines the same straight line $y^L(z)$ should be obtained independent of the actual peak-to-peak width $\Delta B_{\text{p.p.}}$. Evidently, the results recorded for $X = PF_6$ at 120 K support a Lorentzian line shape as far as seven times $\Delta B_{\text{p.p.}}$ into the line wings (Fig. 4).

The analysis of the variation of the linewidth with orientation and temperature (see Fig. 5 for $AsF_6$) shows that the line becomes narrower with decreasing temperature in the metallic phase. The variation of the linewidth with the orientation in the magnetic field has the shape typical for a dipolar interaction of two spins, which belong to the same stack.[25] The linewidth becomes increasingly anisotropic with increasing temperature in the metallic phase. The same result was obtained for $X = PF_6$.

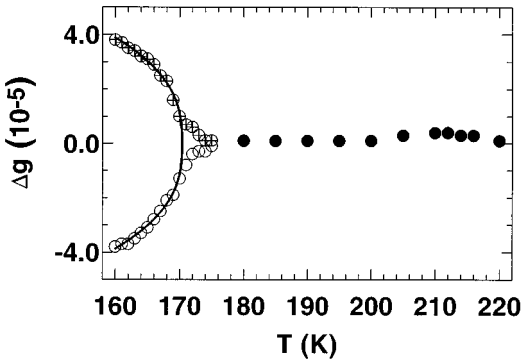


FIG. 6. Variation of the *g* factor with the temperature at the structural phase transition $T_r$ of $(PE)_2AsF_6 \cdot \frac{2}{3}THF$. Since some stacks or parts of the stacks turn right and the others left, the line splits up into two lines. The fixed orientation was chosen in that way that at 160 K the two lines were separated as much as possible with $c \perp \mathbf{B}_0$. The solid lines are fitted curves (see Sec. IV A).

#### *3. Structural phase transition ($T_r$)*

If the crystal is oriented in the magnetic field with $\mathbf{B}_0 \perp c$ and $\angle(\mathbf{B}_0, b) \simeq 45°$, the ESR line splits up into two lines when cooling down below a characteristic temperature $T_r$. Figure 6 shows the variation of the *g* factor of a $(PE)_2AsF_6 \cdot \frac{2}{3}THF$ crystal with the temperature.

To learn more about the molecular reorientation we cooled the crystal down to 140 K and analyzed the angular variation of the *g* factor, using *c* as the axis of rotation. The result is shown in Fig. 7. Obviously the two ESR lines show the same angular variation of their *g* factors within the error limit. Only the principal axes of the *g* tensor are rotated against each other. The difference is 6.85° for this crystal, but values up to 9.3° for other $(PE)_2AsF_6 \cdot \frac{2}{3}THF$ crystals were found. For $(PE)_2PF_6 \cdot \frac{2}{3}THF$ crystals we found 2.8° and 5.3°. The angular variation itself corresponds to spins on perylene molecules of the stacks. This means that at this phase transition $T_r$ stacks or parts of the stacks turn right and the others left around the stacking axis.

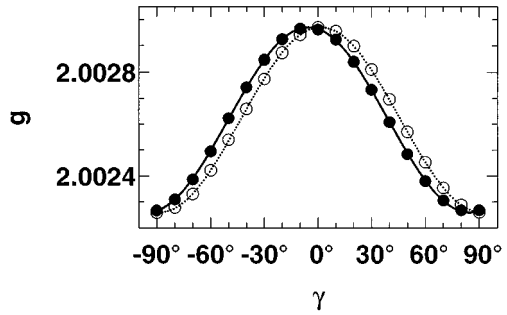


FIG. 7. Angular variation of the *g* factor of the two lines of Fig. 6 at 140 K for rotation around *c*. The solid lines are fitted curves (see text).

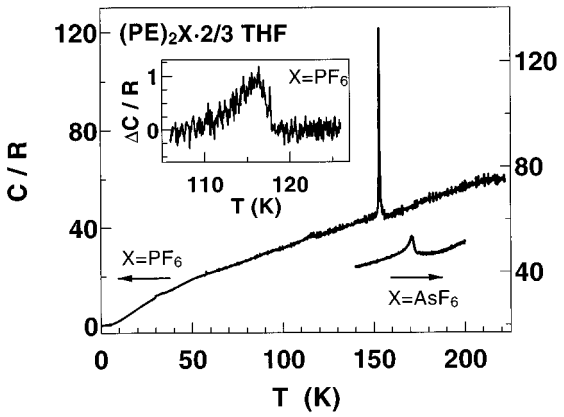


FIG. 8. Variation of the molar heat capacity of $(PE)_2PF_6\cdot\frac{2}{3}THF$ and $(PE)_2AsF_6\cdot\frac{2}{3}THF$ with temperature. The peaks at 153 K and at 171 K, respectively, are the result of the structural phase transition in the metallic range. The inset shows on an expanded scale the data between 100 K and 130 K for $(PE)_2PF_6\cdot\frac{2}{3}THF$ after subtraction of the background contribution of the lattice to the heat capacity. The anomaly in this temperature region is caused by the Peierls transition, and is only barely visible without this expansion. The anomaly in the specific-heat at the Peierls transition of $(PE)_2AsF_6\cdot\frac{2}{3}THF$ was too small to be detected.

The ratio of the intensities of the two lines was nearly 1:1 for the crystal, whose results are shown here, but it depends on the chosen crystal. We also encountered one crystal with an intensity ratio of 6:1.

In the measurement displayed in Fig. 6 the single line above 180 K and the two lines below 160 K have a linewidth of about 21 mG. In the region of $T_r\pm 10$ K the lines are broadened to about 30 mG just below $T_r$. The observed broadening at the transition is likely to be a result of fluctuations of the angle of rotation or of distribution of the transition temperature, but not to be caused by a comparable change of the relaxation time $T_2$.[17] At another measurement with the same crystal we could observe more than two lines in the transition range, which is another hint for the distribution of transition temperatures and for fluctuations of the angle of rotation. Overlap of the lines close to $T_r$ prevented a more detailed analysis. No angular variation of the linewidths at 140 K for rotation around the $c$ axis was found.

The variation of the molar heat capacity with the temperature is shown in Fig. 8. The data of $(PE)_2PF_6\cdot\frac{2}{3}THF$ reveal a ''clear peak'' at $153\pm 0.3$ K and that of $(PE)_2AsF_6\cdot\frac{2}{3}THF$ a smaller one at $171.5\pm 0.3$ K. The same difference in significance and transition temperature was observed for the microwave conductivity and the static magnetic susceptibility (see Fig. 2).[14]

Neither the transition temperature $T_r$ nor the shape of the anomaly in the specific-heat depends on the heating rate. At a phase transition of first order a ''latent heat'' appears. For this reason a phase transition of first order should depend on the heating rate. Since the peaks in the heat capacity of $(PE)_2X\cdot\frac{2}{3}THF$ were independent of the heating rate, the structural phase transition in the metallic phase must be of second order. The continuous variation of the $g$ factors in Fig. 6 is also a sign for a transition of second order.

The enthalpy of the transition is $(340\pm 10)$ J/mol for $(PE)_2PF_6\cdot\frac{2}{3}THF$ and about (400–550) J/mol for $(PE)_2AsF_6\cdot\frac{2}{3}THF$. These results correspond to a change in the entropy of $(0.38)R\ln 2$ for $(PE)_2PF_6\cdot\frac{2}{3}THF$ and $(0.45)R\ln 2$ for $(PE)_2AsF_6\cdot\frac{2}{3}THF$, respectively. It is well known[14] that there is considerable thermal motion and disorder in the perylene packing as well as in the $X$ groups and in the built-in THF solvent molecules at room temperature. It is possible that at the phase transition the THF molecules freeze in one of two possible orientations in the system. A lower transition entropy than $R\ln 2$ would be expected at such an order-disorder transition, due to the reduced molar THF content of these salts.

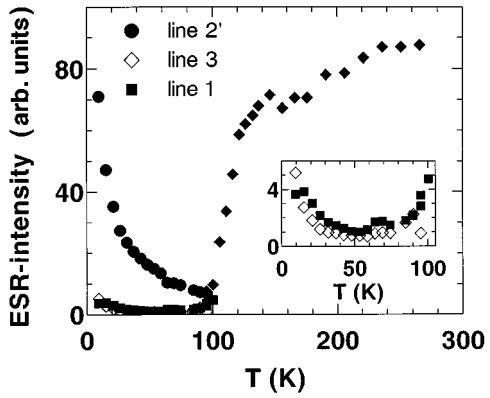


FIG. 9. ESR intensities of $(PE)_2PF_6\cdot\frac{2}{3}THF$ (sample 66a1). Below 95 K intensities were determined by a three-line fit; the line denoted by $2'$ can be further decomposed using information obtained in other orientations. The inset shows the lines of weaker intensity on an expanded scale. Note that line 1 changes from Curie-type behavior at low temperatures to increase of intensity near $T_P$.

### B. Peierls transition

We present the phenomena observed in the course of the Peierls transition for $(PE)_2PF_6\cdot\frac{2}{3}THF$ as an example. [For $(PE)_2AsF_6\cdot\frac{2}{3}THF$ the increase in ESR linewidth below $T_P$ is by far less pronounced as for $(PE)_2PF_6\cdot\frac{2}{3}THF$.] Besides the very pronounced anomaly at 153 K the specific-heat curve shows a further structure at $T_P=118$ K (inset of Fig. 8). Conductivity and magnetic susceptibility (see Fig. 2) both show a steep decrease (with falling temperature) below $T_P$, thus confirming that this second anomaly corresponds to the Peierls transition.[14] Figure 9 shows the temperature dependence of the ESR intensity. In the high-temperature metallic range above $T_P$ essentially the CE ESR is observed. Here the increase of intensity with temperature indicates the presence of fluctuations announcing the Peierls transition. These fluctuations persist between $T_P$, the temperature of three-dimensional ordering in real quasi-one-dimensional systems, and $T_P^{\mathrm{MF}}$, the transition temperature given by a mean-field calculation for a strictly one-dimensional system.[3] Below $T_P$ a steep decrease of the susceptibility due to the opening of the energy gap is observed. The analysis of the static magnetic susceptibility allowed one to follow the opening of the gap in detail.[14] Fitting, as suggested by mean field calculations, a scaled BCS-type gap $\Delta_{\mathrm{BCS}}(T=0)$ and $T_P$ were obtained: $\Delta_{\mathrm{BCS}}=33.7$ meV, $T_P=118$ K and $\Delta_{\mathrm{BCS}}=26.1$ meV, $T_P=102$ K for $(PE)_2PF_6\cdot\frac{2}{3}THF$ and $(PE)_2AsF_6\cdot\frac{2}{3}THF$, respectively.

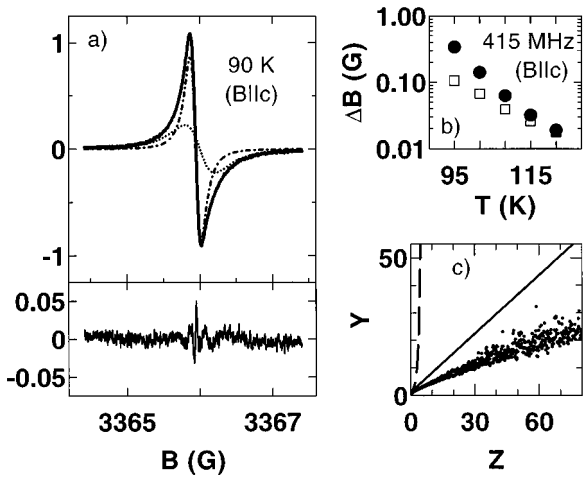


FIG. 10. Spectrum of $(PE)_2PF_6 \cdot \frac{2}{3}THF$ (sample 66a1) at 90 K, $\mathbf{B}_0 \| c$ , 9.5 GHz, normalized units: (a) spectrum, two-line fit, lines 1 and 2, whose sum was fitted (top) and difference of spectrum and fit on enlarged scale (bottom), (b) temperature dependence of the width of lines 1 and 2 near the Peierls transition (415 MHz), and (c) spectrum transformed accordingly to Eq. ( 3).

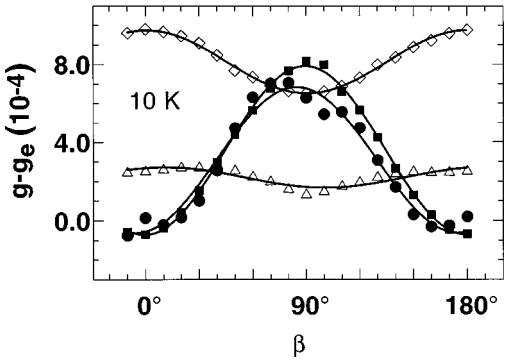


FIG. 11. $g$ anisotropy of the four types of defects of $(PE)_2PF_6 \cdot \frac{2}{3}THF$ at 10 K (sample 66a1) at 9.5 GHz. Sample was turned around the $b$ axis; $g_e$ denotes the free electron $g$ factor. Solid symbols refer to defect types 1 (squares) and 2 (circles), which interact with the conduction electrons present at higher temperatures. Defect types 3 and 4 (open symbols) are not considered in further detail. For linewidths and intensity ratios see Table II.

Below the Peierls transition the ESR linewidth (peak to peak) increases by a factor of about 100. The increase of the dipolar contribution is even more pronounced, reaching a factor of about $10^3$ (see in detail Secs. III D and IV B). A deviation from the Lorentzian line shape observed in the metallic range evolves. Figure 10 gives an example for a spectrum and the analysis of its line shape at 90 K. The spectrum transformed by Eq. (3) is shown together with a transformed Gaussian and Lorentzian line in Fig. 10(c). The line shape is neither Gaussian nor Lorentzian. On the other hand, it is well described as the sum of two Lorentzian lines. This is proved by the small difference between data and two-line fit given in the lower part of Fig. 10(a). The narrower and broader of these two lines will be denounced by 1 and 2, respectively. The resulting linewidths are given in Fig. 10(b). At about 60 K the intensity variation of the two lines turns from the steep decrease directly below $T_P$ to a Curie-type temperature dependence (see, for example, solid symbols in the inset of Fig. 9). It is a crucial point of the analysis that the same lines 1 and 2 can be followed through the temperature range from 10 K to $T_P = 118$ K. Thereby their character changes steadily from that of localized defects at low temperatures to that of conduction electrons near and above the Peierls transition (see also Sec. III D). At low temperatures two more lines 3 and 4 can be detected, whose intensities show Curie-type behavior. At $\mathbf{B}_0 \| c$, the orientation examined for Fig. 9, lines 2 and 4 coincide. Therefore for the analysis of the susceptibility only a three-line fit to the spectra was performed. (In Fig. 9 the common line describing line 2 and 4 is denoted by $2'$.)

### C. Low-temperature paramagnetic defects

#### *1. Experimental facts*

Before studying the combined interacting system of conduction electrons and defects for $T$ approaching $T_P$, the low-temperature defects alone are considered. The Curie contribution to the static susceptibility found for $(PE)_2PF_6 \cdot \frac{2}{3}THF$ and $(PE)_2AsF_6 \cdot \frac{2}{3}THF$ corresponds to $1.76 \times 10^{-3}$ and $1.23 \times 10^{-3}$ spins $S = 1/2$ per formula unit, respectively.[14] For further characterization of the defects of $(PE)_2X \cdot \frac{2}{3}THF$ at 10 K, where no conduction electrons are present, three series of spectra have been taken turning around $b$ and $c$ and in the $b$-$c$ plane. The rich information represented by the structured spectra of each series allows an unambiguous decomposition of the spectra in four (five) Lorentzian lines for $X = PF_6$ ($AsF_6$). Imposing the ratio of intensities to be constant for each series permitted us to reduce the number of fit parameters considerably.[18] The resulting $g$ anisotropy of the four types of defects for $(PE)_2PF_6 \cdot \frac{2}{3}THF$ is shown in Fig. 11 for rotation around $b$. Two types of behavior can be distinguished: Line 1 (solid squares) and line 2 (solid circles) show to a good approximation the $g$ anisotropy of a perylene molecule, which is part of the stack. The $g$ anisotropy of line 3 (open rhombs) and line 4 (open triangles) is considerably weaker. Turning around $c$ and in the $b$-$c$ plane their $g$ factor was constant. This excludes the assumption that the corresponding spins of types 3 and 4 reside on the PE molecules forming the ''walls'' between the stacks. The widths of the defect lines show no pronounced angular variation (Table II). The same four types of defects were found for three samples of $(PE)_2PF_6 \cdot \frac{2}{3}THF$ produced using perylene of a different origin and hence different impurity content before zone refining. It is a remarkable difference between $(PE)_2PF_6 \cdot \frac{2}{3}THF$ and $(PE)_2AsF_6 \cdot \frac{2}{3}THF$ that the $g$ anisotropy of the type-2

TABLE II. Defect lines of $(PE)_2PF_6 \cdot \frac{2}{3}THF$. Linewidth of sample 66a at 10 K in two orientations. Intensity fixed for all fits of Fig. 11 is given in percent of the overall intensity.

| | $\Delta B(\mathbf{B} \| c)$ (G) | $\Delta B(\mathbf{B} \perp c)$ (G) | Intensity |
|---|---|---|---|
| Line 1 | 0.47 | 0.66 | 5% |
| Line 2 | 2.6 | 2.4 | 39% |
| Line 3 | 0.84 | 1.0 | 9% |
| Line 4 | 1.3 | 1.4 | 47% |

defects of $(PE)_2AsF_6 \cdot \frac{2}{3}THF$ is that of PE molecules which are also part of the stacks, but rotated 90° around the *c* axis.

Turning on the CE susceptibility by increasing the temperature drastically changes the linewidth and intensity of lines 1 and 2, while lines 3 and 4 remain unaffected. There exists a dipolar and exchange interaction between defect types 1 and 2 and the conduction electrons (Sec. IV B). Since exchange is a short-range interaction and the angular dependence of the *g* value and linewidth is characteristic for a dipole-dipole interaction of PE radical spins on the same stack, defects 1 and 2, and the CE must be part of the same stacks.

#### *2. Interpretation*

Two types of intrinsic defects should occur in a system like $(PE)_2X \cdot \frac{2}{3}THF$, showing a Peierls transition. A solitonlike defect can be imagined as a mobile domain boundary separating regions with different spatial phases of the Peierls distortion. The phase mismatch between the domains is resolved over several intermolecular distances, which gives the extension of the ''soliton.'' At the origin of the phase mismatch may be the finite stack length in real systems, which in general will not be an integer multiple of the period of the Peierls distortion. Also, structural defects may fix the phase at different sites in a way that is not compatible with the period of the Peierls distortion. For charge-density-wave systems solitons with spin-charge combinations of ($S=\frac{1}{2}$, $Q=0$) and ($S=0$, $Q=\pm e$) have been predicted.[27,31–33]

We interpret defect type 1 as a spin carrying ''soliton'' whose delocalization and mobility average the hyperfine interaction. This leads to a much smaller linewidth of defect type 1 in comparison with type 2. Additional support for this interpretation comes from the fact that the same type of defect (very narrow line, *g* factor of stack molecules) has been observed in other systems showing a Peierls transition like $(\text{fluoranthene})_2PF_6$ (Refs. 26 and 28) or in $(PE)_2AsF_6 \cdot \frac{2}{3}THF$ and $(PE)_2PF_6 \cdot \frac{2}{3}THF$ grown from perylene purified by sublimation which show otherwise markedly different defect spectra. At the end of a finite stack a local deviation from the 2:1 stoichiometry can lead to a localized spin. Likewise a phase mismatch may be not resolved at the interior of a stack, but at its end. Defect type 2, showing the larger linewidth, is identified with this kind of localized defect at the end of the finite stack. We assume that the defects of types 3 and 4 are found in a surface layer, which explains the lack of interaction with the conduction electrons. Even freshly grown samples often show an insulating surface layer. Aging the sample by heating it to 60 °C considerably increased the intensity of line 4. The *g* factor of the aging product lies close to the directional average of the *g* tensor of perylene radical cations and the principal values of the *g* tensor have been indentified recently from the orientational average by high-frequency ESR (90 GHz). We will not consider the defect ESR lines 3 and 4 in further detail.

### D. Electron-spin-resonance linewidth in the low-temperature phase

Around 60 K the Curie-type behavior governing the intensities of lines 1 and 2 at low temperatures changes to the increase observed directly below the Peierls transition while lines 3 and 4 continue to show a Curie-type behavior until they are lost due to comparatively weak intensity and large linewidth. The evolution of the width of lines 1 and 2 in this range is shown in Fig. 12. At 60 K and 65 K the weak angular dependence and the absolute value of both linewidths are still very similar to that of defect types 1 and 2 at 10 K. A drastic change in behavior is observed at 70 K with the onset of an angular dependence characteristic for the magnetic dipolar interaction of spins on the same stack. Here besides defects also conduction electrons start to contribute to the intensities. Since at the same time the linewidths become anisotropic, we conclude that it is the dipolar interaction of the defects with the CE spins that causes the angular dependence of the width of lines 1 and 2. The angular-dependent part of the linewidths decreases with increasing temperature (Fig. 12) and almost vanishes at the Peierls transition. This confirms that we do not observe broadening by a dipole-dipole-interaction between CE spins: For KCP $[K_2Pt(CN)_4Br_{0.3}]$ that type of interaction was found to increase with temperature below $T_P$ since the mean distance between thermally activated conduction electrons decreases.[29] It should also be noted that in addition to the defect lines already present at lower temperatures no particular CE lines appear above 70 K. Their absence and the fact that the intensities of lines already present at lower temperatures increase lead to the conclusion that besides a dipolar interaction also an exchange interaction between defects and conduction electrons is present. This exchange coupled system appears in the ESR as a single line. In $(PE)_2X \cdot \frac{2}{3}THF$ for

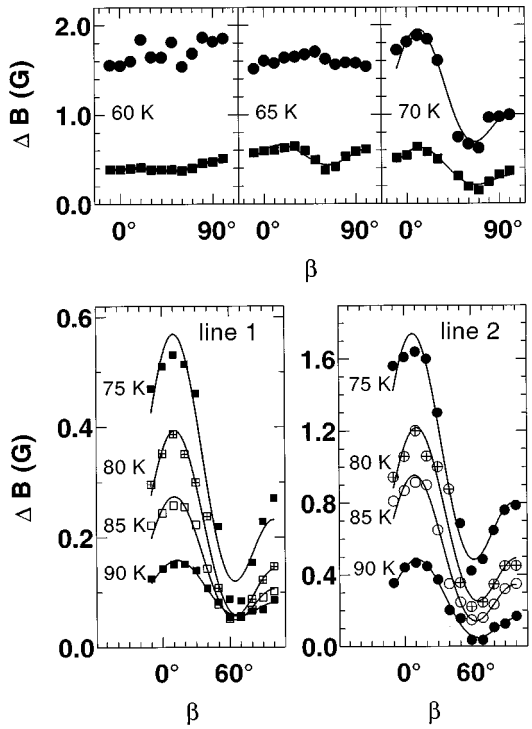


FIG. 12. Angular dependence of the width of lines 1 and 2 of $(PE)_2PF_6 \cdot \frac{2}{3}THF$ (sample 66a1) at 9.5 GHz. Sample was turned from $\mathbf{B}_0 \| c$ to $\mathbf{B}_0 \perp b,c$ . Note the appearance of the variation characteristic for the dipolar interaction at 70 K (top). Lines 1 and 2 shown on different scales (bottom).

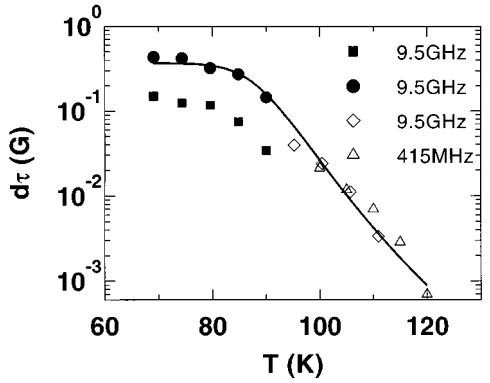


FIG. 13. Product of correlation time and strength of the dipolar interaction for $(PE)_2PF_6 \cdot \frac{2}{3}THF$ (sample 66a1). 70–90 K, results for lines 1 and 2 separately; 95–120 K, results of one-line-fits; triangles 415 MHz; other symbols 9.5 GHz.

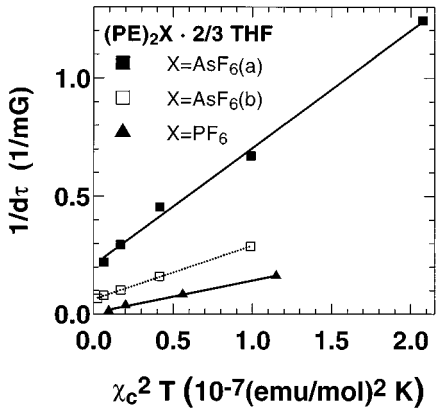


FIG. 14. Inverse of the product of correlation time $\tau$ and strength of the dipolar interaction $d$ as a function of $\chi_C^2 T$. Variation for $(PE)_2PF_6 \cdot \frac{2}{3}THF$ (solid triangles) agrees with Eq. (12). For both samples of $(PE)_2AsF_6 \cdot \frac{2}{3}THF$ (squares) an additional constant term has to be added [Eq. (13)].

$X = PF_6$ as well as for $X = AsF_6$ both defect types 1 and 2 give rise to a line of that type. Near the Peierls transition the widths of lines 1 and 2 tend to be equal, so that a description with one Lorentzian line becomes appropriate. The angular dependence of the width of this single line for $(PE)_2AsF_6 \cdot \frac{2}{3}THF$ at temperatures near below $T_P$ was shown in Fig. 5.

The solid lines in Figs. 5 and 12 are fits of Eq. (4), an expression already applied to $(\text{fluoranthene})_2 PF_6$:[26]

$$\Delta B = \Delta B_0 + d\{\tfrac{3}{8}[1-3\cos^2(\beta)]^2 J(0) + \tfrac{15}{4}\sin^2(\beta)\cos^2(\beta)J(\omega) + \tfrac{3}{8}\sin^4(\beta)J(2\omega)\}, \quad (4)$$

with

$$d = \frac{\gamma^3 \hbar^2 s(s+1)}{a^6} P \quad (5)$$

and

$$J(\omega) = \frac{2\tau}{1+\omega^2\tau^2}. \quad (6)$$

It is the sum of a constant term $\Delta B_0$ describing the linewidth due to a hyperfine interaction and relaxation by the Elliot mechanism and an angular-dependent term. The latter has been calculated for the interaction of magnetic point dipoles. $\beta$ is the angle between the separation line of the point dipoles and the magnetic field vector. In Eq. (5) we introduced the probability $P$ of the interacting spins being situated on neighboring molecules with the intermolecular distance $a$. From a line shape analysis we have no evidence that one-dimensional diffusive spin dynamics is responsible for relaxation (Sec. III A 2). Therefore we assume a simple exponential decay of the correlations of the dipolar interaction with a correlation time $\tau$ leading to the spectral density given by Eq. (6).

Parameters of the fit are $\Delta B_0$, $d\tau$, and $\tau$. The more realistic assumption of an extended spin density instead of point dipoles changes significantly the linewidth in the orientation $\mathbf{B}_0 \perp b,c$ and hence the weight of the nonsecular frequency-dependent terms in the fit of Eq. (4). Therefore a reliable absolute value of $\tau$ alone is not obtained.[26] Anyway at 9.5 GHz for the data shown in Fig. 12 $\omega^2\tau^2 \gg 1$ so that the nonsecular terms can be neglected. In summary the fits allow us to follow the parameter $d\tau$ as a function of temperature. These data, plotted in Figs. 13 and 14, will be analyzed based on a theoretical model in Sec. IV B.

## IV. THEORY AND INTERPRETATION

### A. Structural phase transition in the metallic phase

Additional information on the structural phase transition of the $(PE)_2X \cdot \frac{2}{3}THF$ salts at $T_r$ can be obtained from an analysis of the temperature dependence of the molecular reorientation. Ginzburg and Landau asserted that the state below the transition temperature $T_c$ of a phase transition is characterized by an order parameter, which vanishes above $T_c$. The experimental results (Sec. III A 3) show that the direction of the axis with the largest value of the $g$ tensor is changed below the transition temperature $T_r$. So the order parameter for this phase transition is reflected by the angle of rotation, which is zero above $T_r$ and unequal to zero below $T_r$. The change of an order parameter with the temperature just below $T_c$ can be approximated by a power law:

$$\Delta\gamma \sim \left(\frac{T_c - T}{T_c}\right)^{\beta}. \quad (7)$$

Since the conditions of the measurement had been $\mathbf{B}_0 \perp c$ and $\gamma \approx 45°$, we can linearize $\Delta g \approx (dg/d\gamma)\Delta\gamma$. So Fig. 6 reflects the characteristics of the order parameter at the phase transition. The solid line is the power law, which was fitted to the averaged curve of the two measured dependences with $\Delta g > 0$ and $\Delta g < 0$. Due to the distribution of transition temperatures and the limited $g$ resolution, the measured curve is pretty much rounded near $T_r$ and thus the determination of the critical exponent is not very accurate. Actually we got $0.377 < \beta < 0.457$ and $170.39\ \text{K} < T_c < 170.64\ \text{K}$. Despite the limited accuracy, $\beta$ is definitely below 0.5, the value predicted by Landau theory for second-order phase transitions. For the determination of $\beta$ in the Landau theory any fluctuations are neglected. A critical exponent $\beta$ below the value of

0.5 of the Landau theory shows that fluctuations cannot be neglected for the observed structural phase transition. This is in accordance with the extended range of pretransitional deviations observed in the microwave conductivity (Fig. 2).

### B. Magnetic-dipolar interaction between conduction electrons and defects

#### 1. Bottleneck model

As for the well-known (fluoranthene)$_2$PF$_6$ we explain the relaxation of the CE spins in the low-temperature phase of (PE)$_2X\cdot\frac{2}{3}$THF within a model based on the interaction between CE spins and localized paramagnetic defects.[26] Since both contribute to the same common Lorentzian-shaped lines, they are coupled by strong exchange interaction. More precisely, strong means that the relaxation between CE spins and defects caused by an exchange interaction is much faster than relaxation to the lattice. In this situation the comparatively weak coupling with the lattice presents a bottleneck in the relaxation path of CE spins and defects. The bottleneck situation present in (PE)$_2X\cdot\frac{2}{3}$THF permits a simple description of exchange narrowing in the coupled system of defects and conduction electrons.

Neglecting the relaxation to the lattice no net energy transfer between conduction electrons and defects occurs. This is expressed by the detailed-balance relation for the relaxation rates:

$$\left(\frac{1}{T_1}\right)_{DC}\chi_D=\left(\frac{1}{T_1}\right)_{CD}\chi_C\,. \tag{8}$$

$DC$ denotes relaxation from defects to the CE, $CD$ the inverse; $\chi_D$ and $\chi_C$ are the susceptibilities of the defects and CE, respectively. The correlations of the dipolar interaction vanish because defects and the CE relax [Eq. (9)]. In the case of the dominating CE susceptibility $\chi_C\gg\chi_D$ it is the faster relaxation of the defects which modulates the dipolar interaction [Eq. (10)]. In analogy to the relaxation of nuclei in a metal, the relaxation of the localized defects is calculated by the Korringa law replacing the hyperfine constant by the exchange constant $J$ [Eq. (11)]:[30]

$$\frac{1}{\tau}=\left(\frac{1}{T_1}\right)_{DC}+\left(\frac{1}{T_1}\right)_{CD} \tag{9}$$

$$\approx\left(\frac{1}{T_1}\right)_{DC} \tag{10}$$

$$=\frac{\pi}{\hbar\mu_B^4}J^2\chi_C^2k_BT. \tag{11}$$

For the experimentally determined parameter $d\tau$ one obtains

$$d\tau=\frac{8}{3}\,\frac{\gamma^3\hbar^2s(s+1)}{a^6}P\frac{\hbar\mu_B^4}{\pi}\,\frac{1}{J^2\chi_C^2k_BT}. \tag{12}$$

In the case $\chi_C\gg\chi_D$ essentially lines of the CE broadened by the dipole fields of the defects are observed. Therefore $P$ is the probability of a given CE ''seeing'' a defect and hence given by the concentration of the defects. $d$ becomes temperature independent, and the fits of Eq. (4) directly give the temperature dependence of the correlation time $\tau$. In the opposite limit taking for $P$ the CE concentration and replacing in Eq. (10) $(1/T_1)_{DC}$ by $(1/T_1)_{CD}$ results in $d\tau$ independent of temperature.

#### 2. Application near the Peierls transition

From the analysis of the static magnetic susceptibility the CE susceptibility is known.[14] This allows us to test the proposed model by plotting $d\tau$ obtained near below $T_P$ as a function of $\chi_C^2T$ (see Fig. 14). For (PE)$_2$AsF$_6\cdot\frac{2}{3}$THF an additional constant term has to be added to the rate given by Eq. (11), leading to

$$\frac{1}{d\tau}-\left(\frac{1}{d\tau}\right)_0\propto\chi_C^2T. \tag{13}$$

However, the data obtained for (PE)$_2$PF$_6\cdot\frac{2}{3}$THF are in agreement with Eq. (11); i.e., in Eq. (13) the second term on the left may be fixed to zero.

We conclude that in the case of (PE)$_2$AsF$_6\cdot\frac{2}{3}$THF exchange between CE and defects is not the only process modulating the dipolar interaction. A second process is responsible for an additional modulation rate showing no or weak temperature dependence. Decomposition of the spectra obtained for (PE)$_2$AsF$_6\cdot\frac{2}{3}$THF at lower temperatures showed that this additional modulation limits the dipolar broadening of both lines 1 and 2. The striking difference between the evolution of the linewidths of (PE)$_2$PF$_6\cdot\frac{2}{3}$THF and (PE)$_2$AsF$_6\cdot\frac{2}{3}$THF below $T_P$ may be due to motional narrowing. This is suggested by comparison of the microwave conductivity. Below $T_P$ it decreases not as fast, as calculated for a semiconductor from the temperature-dependent gap [Fig. 10(a) and 10(b) of Ref. 14)]. The deviation, which has been ascribed to a collective transport by charge density waves, is much more pronounced for (PE)$_2$AsF$_6\cdot\frac{2}{3}$THF than for (PE)$_2$PF$_6\cdot\frac{2}{3}$THF. This indicates a weaker commensurability pinning and hence a less stable phase of the CDW's in the case of (PE)$_2$AsF$_6\cdot\frac{2}{3}$THF. Since the defects interacting with the conduction electrons are assumed to consist of phase mismatches of the CDW's, a reduced pinning will increase their mobility. This is valid for the mobility of the ''soliton'' as well as for the residual mobility of a defect ''localized'' at a chain end.

Support for the assumption of a weaker pinning potential of (PE)$_2$AsF$_6\cdot\frac{2}{3}$THF comes also from comparison of the ESR-line intensities of the two in-stack perylene like defects 1 and 2. Strong commensurability pinning should hinder the formation of phase mismatches inside the stack, and instead favor defects localized at stack ends. This way the ratio of the intensities at 10 K indicates a weaker pinning in (PE)$_2$AsF$_6\cdot\frac{2}{3}$THF. In the case of (PE)$_2$AsF$_6\cdot\frac{2}{3}$THF the intensities are almost equal (20% and 21%), whereas for (PE)$_2$PF$_6\cdot\frac{2}{3}$THF the wide line 2 is much more intense than line 1 (39% and 5%).

#### 3. Application to hexafluorophosphate salts

The evolution of the correlation time, i.e., the parameter $d\tau$, has been followed in detail for (PE)$_2$PF$_6\cdot\frac{2}{3}$THF as displayed in Fig. 13. Since the intensity of line 2 by far exceeds that of line 1, $d\tau$ obtained by one-line fits near the Peierls

transition (open symbols in Fig. 13) to a good approximation is valid for line 2. Below 90 K, $d\tau$ was determined separately for both lines (fits of solid curves in Fig. 12). In this range, the steep increase observed below $T_P$ turns to an almost temperature-independent behavior. The solid curve in Fig. 13 is a fit of Eq. (13) to the data obtained for line 2. To perform the fit we used for the CE susceptibility the ESR intensity of the same sample. Parameters were $(d\tau)_0$ and the constant of proportionality. Note that the slope of the curve in Fig. 13 is not adjusted. The good agreement of the theoretical slope with the data confirms that a Korringa-type relaxation of the defects accounts for the decay of the correlations of the dipolar interaction. As assumed for the fit an additional modulation rate as found for $(PE)_2AsF_6 \cdot \frac{2}{3}THF$ may be at the origin of the flattening of the curve at low temperatures. However, it should be noted that in this temperature range the assumption $\chi_C \gg \chi_D$ is no longer valid, which may also explain the weak temperature dependence of $d\tau$ (see Sec. IV B 1).

From the data displayed in Fig. 10(b) it can be deduced that near $T_P$ with the width of the lines also the values for $d\tau$ tend to be equal. At lower temperatures $d\tau$ of line 1 rests well below the value obtained for line 2 (Fig. 13). Therefore the overall temperature dependence of $d\tau$ for line 1 is much weaker than for line 2, and it does not follow Eq. (13). It is not unexpected, however, that the relaxation of this fundamentally different, presumably delocalized, and mobile defect shows another temperature dependence.

## V. CONCLUSIONS

In the metallic high-temperature phase of $(PE)_2X \cdot \frac{2}{3}$ THF the perylene stacks change their orientation in the course of a structural phase transition. The angle of rotation behaves as the order parameter of a second-order phase transition. Since there is no broadening due to averaging over different molecular orientations below the transition, on a microscopic scale the stacks remain intact. Also the high anisotropy of the conductivity must be essentially preserved, since otherwise the lines would be substantially broadened by the Elliot mechanism.

The current ESR analysis supports a band filling of $\frac{5}{8}$ of the Brillouin zone corresponding to the mean distance $d$ of the stack molecules. This implies an unusual large periodicity of the Peierls distortion of $8d$. It is of the same order of magnitude as the elastic scattering length calculated from the diffusion constant, obtained by pulsed ESR. Therefore this large periodicity will go along with a less stable distorted phase. This explains the reduced transition temperature of $(PE)_2X \cdot \frac{2}{3}THF$ ($T_P = 102-118$ K) as compared with for example ( fluoranthene)$_2$ $PF_6$ [$T_P = 182$ K (Ref. 6)].

In the low-temperature phase, different paramagnetic defects can be characterized. As with increasing temperature the thermally excited conduction electrons appear, two of the defect lines change their character. Their width becomes angular dependent and decreases with temperature, while their intensity increases. The evolution of these lines can be followed from 10 K up to the Peierls transition. We interpret these defect types as a mobile spin carrying defect of the Peierls distortion (''soliton'') and as a spin localized on PE molecules at the end of finite stacks. In the case of $(PE)_2PF_6 \cdot \frac{2}{3}THF$ the latter molecules are oriented as the stack molecules; in the case of $(PE)_2AsF_6 \cdot \frac{2}{3}THF$ they are rotated 90° around $\hat{c}$ with respect to the stack molecules. When at higher temperatures also conduction electrons are present, ESR detects only the exchange coupled systems that each defect type forms with the conduction electrons. Comparatively strong exchange between conduction electrons and defects leads to a bottleneck situation that allows one to calculate the modulation rate, once the relaxation rate of the defects to the conduction electrons is known. Assumption of a Korringa-type relaxation relates the dipolar broadening to the CE susceptibility:

$$\Delta B_{dd} \propto \frac{1}{\chi_C^2 T}. \tag{14}$$

Equation (14) well describes the increase in linewidth below $T_P$ in the case of the line associated with the chain end defect of $(PE)_2PF_6 \cdot \frac{2}{3}THF$ (line 2). For the much less intense line associated with the ''soliton'' (line 1), the increase is somewhat weaker. Also for $(PE)_2AsF_6 \cdot \frac{2}{3}THF$ the Korringa-type relaxation gives an important contribution to the modulation of the dipolar interaction. However, in this case an additional temperature-independent modulation limits the increase of the dipolar line broadening to much smaller values as for $(PE)_2PF_6 \cdot \frac{2}{3}THF$. This effect is sample dependent and may be related to the comparatively larger microwave conductivity of $(PE)_2AsF_6 \cdot \frac{2}{3}THF$ in the semiconducting phase.

## ACKNOWLEDGMENTS

We are indebted to O. Baillard, M. Burggraf, H. Dragan, A. Flohr, H. Lossau, B. Pilawa, R. Ruf, D. Schweitzer, W. Wendl, T. Wokrina, H. Winter, and A. Zitsch for discussions and experimental contributions. This work was supported by the Deutsche Forschungsgemeinschaft within the Sonderforschungsbereich 195 (Universität Karlsruhe).

[1] Proceedings of the International Conference on Science and Technology of Synthetic Metals (ICSM '94), Seoul, Korea [Synth. Met. **69-71**, 719 (1995)].

[2] D. Jerome and H.J. Schultz, Adv. Phys. **31**, 299 (1982).

[3] S. Kagoshima, H. Nagasawa, and T. Sambongi, *One-Dimensional Conductors* (Springer-Verlag, Berlin, 1988).

[4] U. Köbler, J. Gmeiner, and E. Dormann, J. Magn. Magn. Mater. **69**, 189 (1987).

[5] V. Ilakovac, S. Ravy, J.P. Pouget, W. Riess, W. Brütting, and M. Schwoerer, J. Phys. (France) IV **3**, C2-137 (1993).

[6] W. Riess and W. Brütting, Phys. Scr. **T49**, 721 (1993).

[7] W. Brütting and W. Riess, Acta Phys. Pol. A **87**, 785 (1995).

[8] M. Mehring, in *Low-Dimensional Conductors and Superconductors*, edited by D. Jerome and L.G. Caron, Vol. 155 of *NATO Advanced Study Institute, Series B: Physics* (Plenum, New York, 1987), p. 185.

[9] Th. Schimmel, B. Koch, H.P. Geserich, and M. Schwoerer, Synth. Met. **33**, 311 (1989).
[10] G. Sachs, W. Stöcklein, B. Bail, E. Dormann, and M. Schwoerer, Chem. Phys. Lett. **89**, 179 (1982).
[11] G. G. Maresch, A. Grupp, M. Mehring, J. U. von Schütz, and H. C. Wolf, J. Phys. (Paris) **46**, 461 (1985).
[12] G. Denninger, Adv. Solid State Phys. **30**, 113 (1990).
[13] H. Endres, J. J. Keller, B. Müller, and D. Schweitzer, Acta Crystallogr. C **41**, 607 (1985).
[14] M. Burggraf, H. Dragan, P. Gruner-Bauer, H. W. Helberg, W. F. Kuhs, G. Mattern, D. Müller, W. Wendl, A. Wolter, and E. Dormann, Z. Phys. B **96**, 439 (1995).
[15] A. Wolter, M. Burggraf, H. Dragan, U. Fasol, E. Dormann, H. W. Hellberg, and D. Müller, Synth. Met. **71**, 1957 (1995).
[16] R. Ruf, H. Lossau, and E. Dormann, Synth. Met. **70**, 1215 (1995).
[17] T. Wokrina, Diplomarbeit, Physikalisches Institut Universität Karlsruhe, Germany, 1995.
[18] A. Wolter, Ph.D. thesis, Physikalisches Institut, Universität Karlsruhe, Germany, 1995.
[19] A. Junod, J. Phys. E **12**, 945 (1979).
[20] R. Jäppelt, Diplomarbeit, Physikalisches Institut Universität Karlsruhe, Germany, 1995.
[21] W. Stöcklein, Ph.D. thesis, Universität Bayreuth, Germany, 1985.
[22] W. F. Kuhs, G. Mattern, W. Brütting, H. Dragan, M. Burggraf, B. Pilawa, and E. Dormann, Acta Crystallogr. B **50**, 741 (1994).
[23] J. Ziegler, Diplomarbeit, Physikalisches Institut Universität Karlsruhe, Germany, 1995.
[24] C.P. Poole, in *Electron Spin Resonance*, (Wiley, New York, 1967).
[25] G. G. Maresch, Ph.D. thesis, 2. Physikalisches Institut der Universität Stuttgart, Germany, 1987.
[26] G. Sachs, E. Pöhlmann, and E. Dormann, J. Magn. Magn. Mater. **69**, 131 (1987).
[27] B. Horovitz, in *Solitons*, edited by S. E. Trullinger, V. E. Zakharov, and V. L. Pokrowsky (Elsevier, New York, 1986).
[28] G. Sachs, Ph.D. thesis, Universität Bayreuth, Germany, 1987.
[29] T. Takahashi, H. Doi, and H. Nagasawa, J. Phys. Soc. Jpn. **48**, 423 (1980).
[30] A. J. Heeger, in *Localized Moments and non Moments in Metals: The Kondo Effect*, Solid State Physics Vol. 23 (Academic, New York, 1969).
[31] M. J. Cohen and A. J. Heeger, Phys. Rev. B **16**, 688 (1977).
[32] M. J. Rice, A. R. Bishop, J. A. Krumhansl, and S. E. Trullinger, Phys. Rev. Lett. **36**, 432 (1976).
[33] L. Zuppiroli, in *Highly Conducting Quasi-One-Dimensional Organic Crystals*, Semiconductors and Semimetals Vol. 27, edited by E. Conwell, (Academic, San Diego, 1988), Chap. 7.